ARTICLE OPEN

Check for updates

High efficiency hierarchical porous composite microfiltration membrane for high-temperature particulate matter capturing

Wanyuan Gui [1], Yuhai Qu[2], Yongfeng Liang [1], Yanli Wang[1], Hui Zhang[3], Benli Luan [1,4 ✉] and Junpin Lin [1 ✉]

Porous intermetallic membrane with extensive interconnected pores are potential candidates as functional materials for high-temperature particulate matter (PM) capturing. However, fabrication of intermetallic membrane with a combined performance of high filtration efficiency and high-temperature oxidation resistance remains a challenge. To tackle this issue, a hierarchical micro-/nano-dual-scale sized pores was constructed on the inner cell walls of a porous support through mutual diffusion and chemical reaction. Benefited from its hierarchical micro/nano-dual-scaled pore structural features, the high Nb containing TiAl-based porous composite microfiltration membrane demonstrates ultrahigh $PM_{>2.5}$ removal efficiency (99.58%) and favorable oxidation/sulfidation performance at high temperature. These features, combined with our experimental design strategy, provide insight into designing high-temperature PM filtration membrane materials with enhanced performance and durability.

INTRODUCTION

Heavy and toxic haze pollution poses a serious risk to human health with detrimental effects on global mortality in recent years[1–3]. Particulate matter (PM) emission from cement factories, power plants, and metallurgical industry is a significant source contributing to acute haze formation[4–6], producing particle sizes below 10 μm, and creating serious health concerns[7–11]. To tackle or mitigate the challenge, porous metals[12,13] and porous ceramics[14–16] are widely utilized at high temperatures, where PM is initially released to take full advantage of filtration efficiency. Although these porous materials are effective at capturing $PM_{2.5}$, and PM_{10}[17], they, unfortunately, suffer in application owing to performance-related challenges such as poor corrosion and high-temperature oxidation resistivities, severe brittleness, and unworkability, and significant energy penalty associated with complicated material preparation procedures. As such, it is of considerable significance to develop functional porous materials for high-temperature PM capturing with a simple, highly efficient, and scalable approach.

TiAl porous alloy is expected to be the next-generation microfiltration membrane for potential application in high-temperature gas/solid or liquid/solid two-phase separation, owing to its characteristics of containing a mixture of metallic and covalent bonds that provide sound mechanical properties[18,19], excellent high-temperature oxidation resistance, and corrosion resistance[20,21] at elevated temperatures, particularly at above 600 °C. Unfortunately, the insufficient efficiency of microfiltration membrane severely limits their practical application in capturing Nano-scale PM, resulting in inadequate filtration performance[22,23]. The main cause of this problem for TiAl porous alloy prepared by powder metallurgy is the formation of micro-scaled pore structure rather than a dual-scale integrated micro/nanoporous network structure during high-temperature heat-treatment processing[24–26].

To overcome these limitations, we offer an alternative approach for fabricating porous composite microfiltration membrane (PCMM) with hierarchical micro/mano-dual-scaled pore structure for efficient high-temperature PM capturing. Control of material nanostructure is an effective approach to modify material properties[27–29]. The introduction of $Nano-ZrO_2$ in the high Nb-TiAl system provides a potential solution for high-temperature application because of its high melting point (2700 °C), low coefficient of thermal expansion, and good creep resistance[30,31]. More specifically, a micro-scale porous microstructure was constructed by controlling self-diffusion and mutual diffusion of Ti, Al, Nb powders below 900 °C, followed by building nano-scale pores on the inner surface of cell walls through chemical reaction between the porous support material and the $Nano-ZrO_2$ particles at 900–1350 °C. Benefited from this structural feature, the designed PCMM demonstrates increased high-temperature PM removal efficiency and favorable high-temperature oxidation/sulfidation performance.

RESULTS AND DISCUSSION

### Microstructure evaluation and phase transformation mechanism of PCMM

The crystal structure of Ti-48Al-6Nb porous alloy and the PCMM (with 4 wt.% $Nano-ZrO_2$ addition) are presented in Fig. 1a. The strong signals of $α_2$-Ti_3Al and $γ$-TiAl in PCMM, as characteristic peaks of Ti-48Al-6Nb porous alloy, suggest the formation of high Nb-TiAl-based matrix. The diffraction peaks of $α$-Al_2O_3 occurring in the diffractograms indicate the formation of PCMM. Fig. 1b exhibits the X-ray diffraction (XRD) patterns of PCMM with 4 wt.% $Nano-ZrO_2$ addition and annealed at different temperatures. It can be seen from Fig. 1b that the $TiAl_3$ phase formed by reaction of Ti with Al at 600 °C and subsequently transformed into $TiAl_2$, TiAl, and Ti_3Al phases at a temperature range of 600–900 °C, whereas the $NbAl_3$ phase formed by reaction of Nb with Al and $NbAl_3$ transformed into Nb_2Al phase at temperatures ranging from 900 to 1350 °C, forming a soluble solid in the matrix interior[18,22]. The $Nano-ZrO_2$ react with Ti_3Al and TiAl at the same time to form the Al_2O_3 phase, observable from the intensified diffraction peaks.

[1]National Center for Materials Service Safety; State Key Laboratory for Advanced Metals and Materials, University of Science and Technology Beijing, Beijing 100083, China. [2]School of Materials Science and Engineering, Nanchang University, Nanchang 330031, China. [3]Qian Xuesen Laboratory of Space Technology, China Academy of Space Technology, Beijing, China. [4]Department of Chemistry, Western University, London, Ontario N6A 5B7, Canada. ✉email: bluan@ustb.edu.cn; linjunpin@ustb.edu.cn

W. Gui et al.
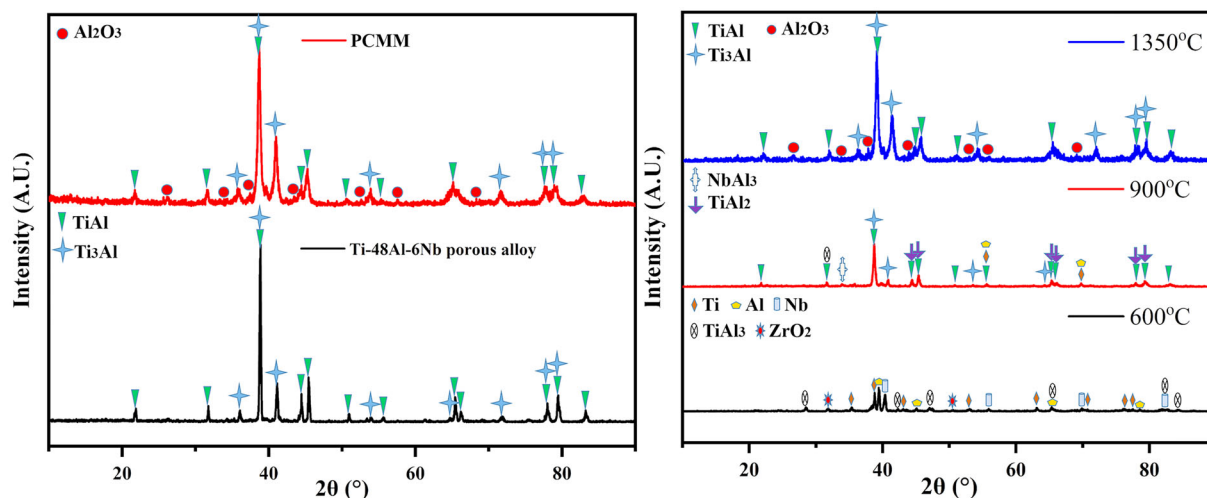
Fig. 1 XRD spectra of porous sample. a Ti-48Al-6Nb porous alloy (black) and PCMM (red); **b** PCMM annealed at different temperatures: 600 °C (black), 900 °C (red), and 1350 °C (blue).
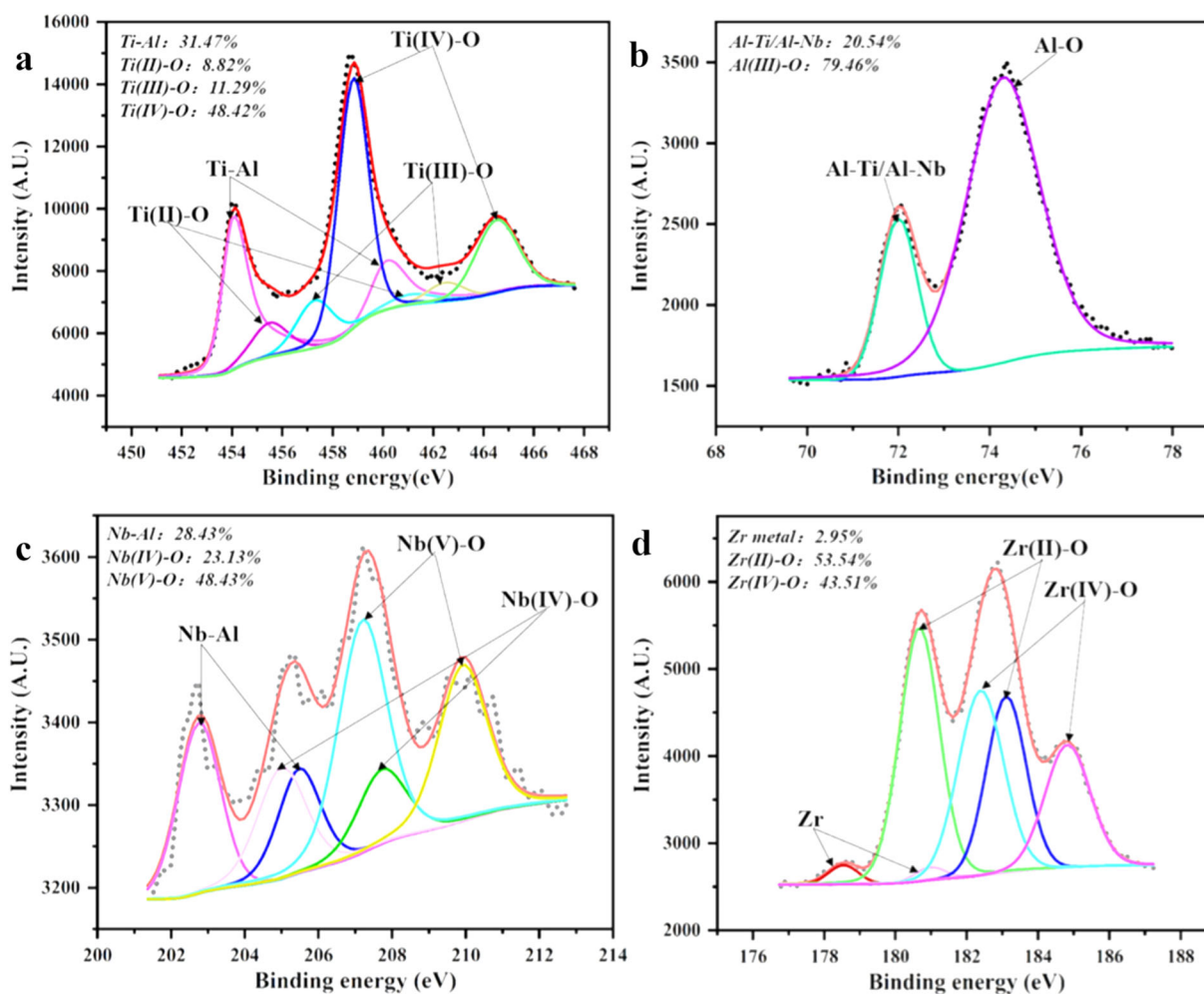
Fig. 2 XPS patterns of PCMM (with 4 wt.% Nano-ZrO$_2$ addition). a *Ti 2p*; **b** *Al 2p*; **c** *Nb 3d*; **d** *Zr 3d*.

XPS analysis was also carried out to investigate the composition of PCMM (Figs 2a–d). *Ti 2p* spectra in the PCMM with 4 wt.% Nano-ZrO$_2$ addition (Fig. 2a) can be divided into two edge splits, *Ti 2p$_{3/2}$* and *Ti 2p$_{1/2}$*, and *Ti 2p* signal suggests that Al and O groups bind to Ti by four coordination modes: The *Ti 2p$_{3/2}$* and *Ti 2p$_{1/2}$* peaks are located 454.06 and 460.16 eV for Ti-Al (TiAl and Ti$_3$Al), 455.50 and 461.10 eV for Ti-O (TiO), 457.3 and 462.5 eV for Ti-O (Ti$_2$O$_3$), 458.82 and 464.52 eV for Ti-O (TiO$_2$)[32,33]. The high-resolution spectra *Al 2p* in the PCMM (Fig. 2b) revealed the presence of Al-Ti/Al-Nb (TiAl and Nb$_2$Al) bonds at 72.00 eV and Al-O (Al$_2$O$_3$) bond at 74.30 eV,
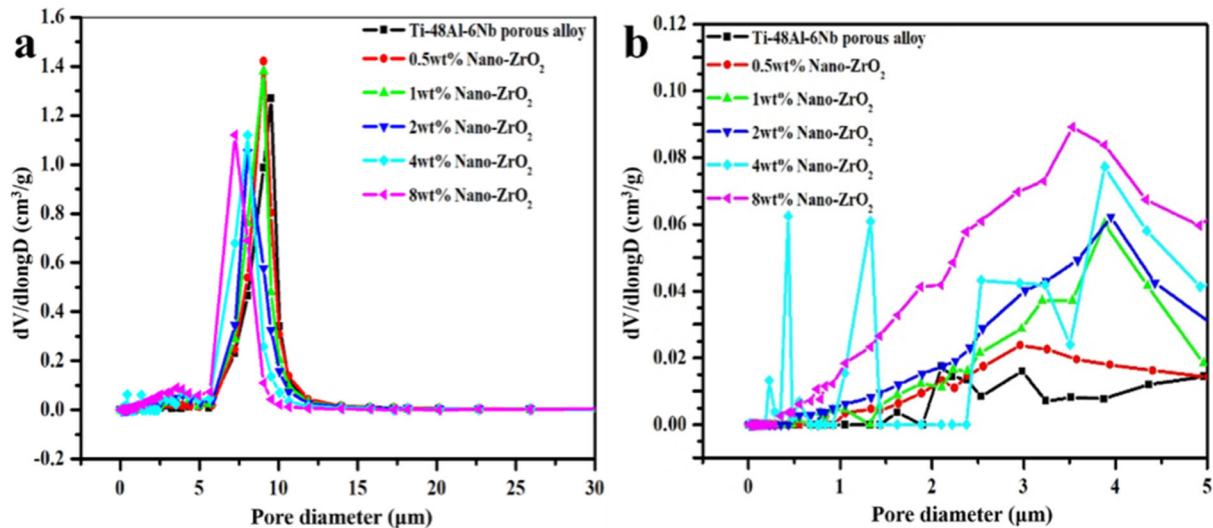
Fig. 3 Pore diameter distribution curve of Ti-48Al-6Nb porous alloy and PCMM. a Ti-48Al-6Nb porous alloy (black) and PCMM with 0.5 wt.% (red), 1 wt.% (green), 2 wt.% (blue), 4 wt.% (cyan) and 8 wt.% (magenta) Nano-ZrO₂ additions; **b** locally magnified curves of Fig. 3a.

Table 1.   Pore parameter for Ti-48Al-6Nb porous alloy and PCMM with different amounts of Nano-ZrO₂ addition (0.5–8 wt.%).
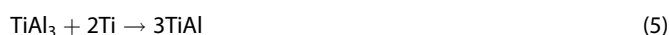
Pore parameter	Ti-48Al-6Nb	0.5 wt.%	1 wt.%	2 wt.%	4 wt.%	8 wt.%
Total pore area (m²/g)	0.05	0.057	0.071	0.077	0.096	0.072
Total pore volume (cm³/g)	0.131	0.156	0.165	0.181	0.197	0.164
Porosity (%)	28.79%	36.91%	39.09%	43.94%	44.78%	39.24%
Density (g/cm³)	3.21	3.96	3.88	4.02	4.07	3.95

suggesting that formation of TiAl, Ti₃Al, Nb₂Al and Al₂O₃ phases[34]. The high-resolution spectra *Nb 3d* in the PCMM (Fig. 2c) can be divided into two edge splits: *Nb 3d₅/₂* and *Nb 3d₃/₂*, with *Nb 3d₅/₂* and *Nb 3d₃/₂* peaks located at 202.7 and 205.48 eV for Nb-Al (Nb₂Al), 205.00 and 207.72 eV for Nb-O (NbO₂), and 207.20 and 209.92 eV for Nb-O (Nb₂O₅), correspondingly[35]. The high-resolution spectra *Zr 3d* in the PCMM (Fig. 2d) revealed the presence of Zr metal at 178.54 and 180.97 eV, and Zr-O (ZrO) bond at 180.68 and 183.11 eV, Zr-O (ZrO₂) bond at 182.39 and 184.82[36]. Therefore, the PCMM (with 4 wt.% Nano-ZrO₂ addition) obtained at 1350 °C are mainly composed of TiAl, Ti₃Al, Nb₂Al, TiO, Ti₂O₃, TiO₂, Al₂O₃, NbO₂, Nb₂O₅, Zr, ZrO, ZrO₂. As such, the phase formation and transformation for the mixture of the Ti-48Al-6Nb matrix and the Nano-ZrO₂ powder heated at different temperatures could proceed as following:
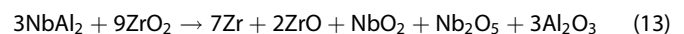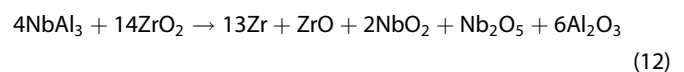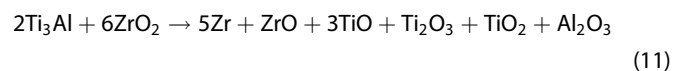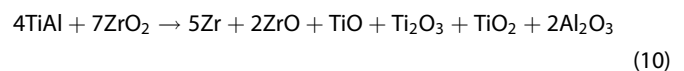
at 600 °C[22]:

$$Ti + 3Al \rightarrow TiAl_3 \tag{1}$$

at 600~900 °C:

$$Nb + TiAl_3 \rightarrow NbAl_3 + Ti \tag{2}$$

$$2TiAl_3 + Ti \rightarrow 3TiAl_2 \tag{3}$$

$$TiAl_3 + 8Ti \rightarrow 3Ti_3Al \tag{4}$$

$$TiAl_3 + 2Ti \rightarrow 3TiAl \tag{5}$$

$$TiAl_2 + 5Ti \rightarrow 2Ti_3Al \tag{6}$$

$$TiAl_2 + Ti \rightarrow 2TiAl \tag{7}$$

at 900~1350 °C:[22,24,26]

$$2TiAl_2 + Ti_3Al \rightarrow 5TiAl \tag{8}$$

$$NbAl_3 + 5Nb \rightarrow 3Nb_2Al \tag{9}$$

$$4TiAl + 7ZrO_2 \rightarrow 5Zr + 2ZrO + TiO + Ti_2O_3 + TiO_2 + 2Al_2O_3 \tag{10}$$

$$2Ti_3Al + 6ZrO_2 \rightarrow 5Zr + ZrO + 3TiO + Ti_2O_3 + TiO_2 + Al_2O_3 \tag{11}$$

$$4NbAl_3 + 14ZrO_2 \rightarrow 13Zr + ZrO + 2NbO_2 + Nb_2O_5 + 6Al_2O_3 \tag{12}$$

$$3NbAl_2 + 9ZrO_2 \rightarrow 7Zr + 2ZrO + NbO_2 + Nb_2O_5 + 3Al_2O_3 \tag{13}$$

The pore parameters are crucially important to the performance of high-temperature PM capturing, especially the pore diameter distribution. The pore diameter distribution of Ti-48Al-6Nb porous alloy and PCMM with 0.5–8 wt.% Nano-ZrO₂ addition analyzed by mercury intrusion porosimeter are exhibited in Fig. 3a and b. Compared with the average pore diameter of Ti-48Al-6Nb porous alloy (9.53 μm), the average pore diameter of PCMM clearly showed a substantial decrease. Regarding the cases at 0.5–8 wt.% Nano-ZrO₂ addition, the minimum average pore diameter (7.25 μm) was achieved when adding 8 wt.% Nano-ZrO₂, and the cumulative pore volume for the smaller pores of 0 ~ 5 μm also increased. This phenomenon could be attributed to the fact that the Nano-sized pores were fabricated on the inner cell walls of high Nb-TiAl support through chemical reaction between TiAl/Ti₃Al and Nano-ZrO₂ at high temperature (>900 °C). In addition, Table 1 quantitatively presents the effect of Nano-ZrO₂ mass on the total pore volume and area, porosity, and the density of PCMM.
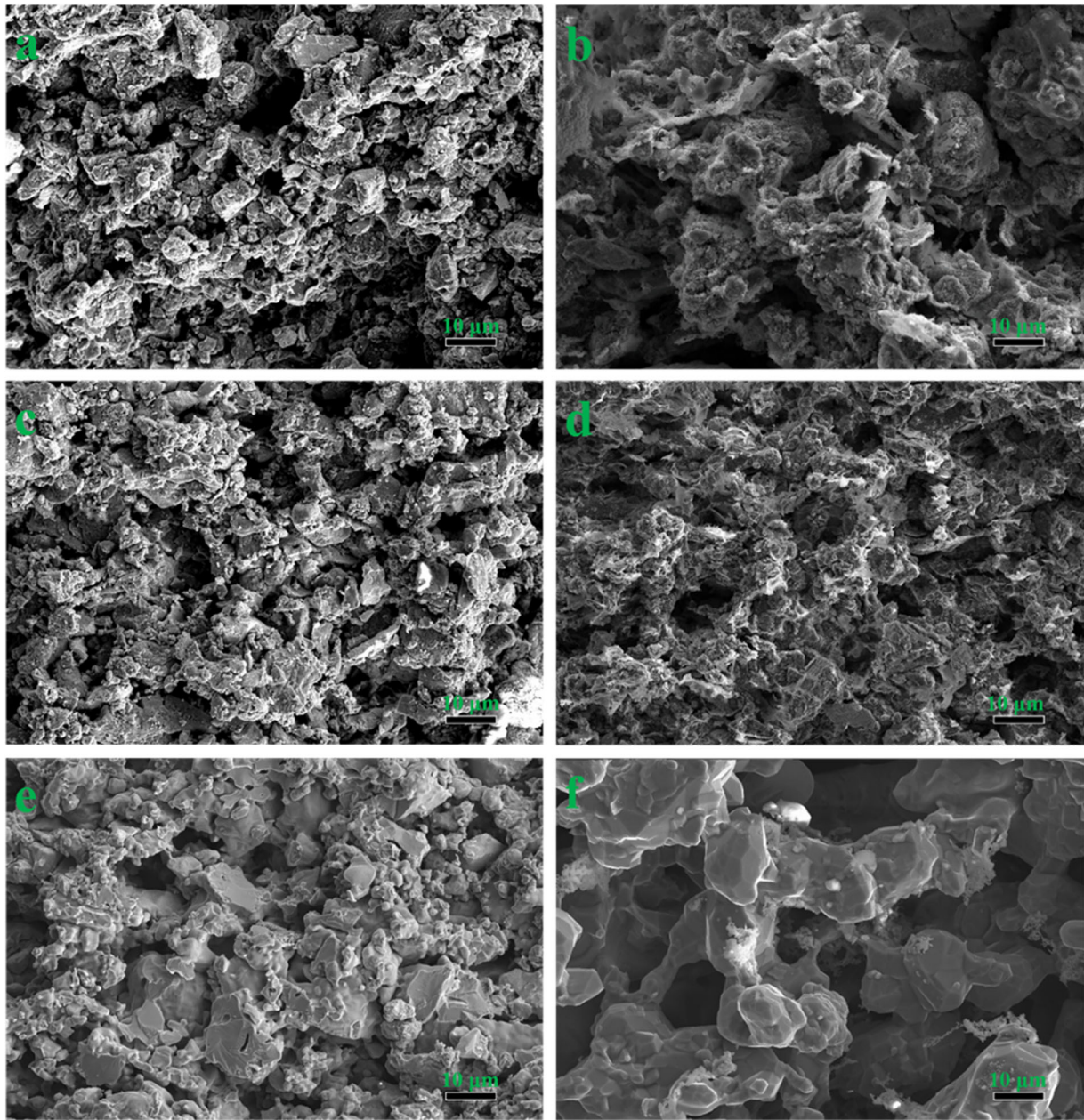
Fig. 4 Surface FESEM images of porous sample. Ti-48Al-6Nb porous alloy at various heat-treatment temperatures: **a** 600 °C, **c** 900 °C, **e** 1350 °C; PCMM at various heat-treatment temperatures: **b** 600 °C, **d** 900 °C, **f** 1350 °C.

Compared with the Ti-48Al-6Nb porous alloy, the total pore area extended from 0.05 m^2/g to 0.096 m^2/g, the total pore volume reached from 0.131 cm^3/g to 0.196 cm^3/g, whereas the porosity increased from 28.79% to 44.78% for the PCMM with 4 wt.% Nano-ZrO$_2$ addition. It is interesting to note that the addition of Nano-ZrO$_2$ can change the minimum pore diameter of Ti-48Al-6Nb porous alloy while improving other pore parameters.

The pore formation and distribution are presented in Fig. 4 and Fig. 5, and the detailed pore parameters of the PCMM heat-treatment at different temperatures (600 °C, 900 °C, 1000 °C, 1100 °C, 1200 °C, 1350 °C) are listed in Table 2. Fig. 4 depicts typical surface field emission scanning electron microscopy (FESEM) images of Ti-48Al-6Nb porous alloy and PCMM with 4 wt.% Nano-ZrO$_2$ addition heated at 600 °C, 900 °C, and 1350 °C, showing the formation of a skeleton structure consisting of particles and possibly Kirkendall voids at 600 °C (Fig. 4a), 900 °C (Fig. 4c). and 1350 °C (Fig. 4e)[22,24]. Similar Kirkendall voids

formation is also observable from the samples of PCMM with 4 wt.% Nano-ZrO$_2$ addition (Fig. 4b and Fig. 4d). Fig. 4f shows the micro/nano-pore formation on the inner cell walls of high Nb-TiAl porous supporting, featuring a hierarchical micro/nano-dual-scaled porous structure, possibly through chemical reaction of Nb-TiAl with Nano-ZrO$_2$ at 900–1350 °C.

The pore diameter distribution of the PCMM with 4 wt.% Nano-ZrO$_2$ addition at various heat-treatment temperatures (600 °C, 900 °C, 1000 °C, 1100 °C, 1200 °C, 1350 °C) are presented in Fig. 5, further illustrating the relationship between micro-structure and heat-treatment temperatures. By increasing the heat-treatment temperature from 600 °C to 1350 °C, the average pore diameter of PCMM continues to increase. More specifically, the average pore diameter increases from 3.22 µm to 3.95 µm when temperature was elevated from 600 to 900 °C due possibly to the mutual diffusion between Ti and Al, and between Nb and Al, along with the transformation of TiAl$_3$ into TiAl and Ti$_3$Al
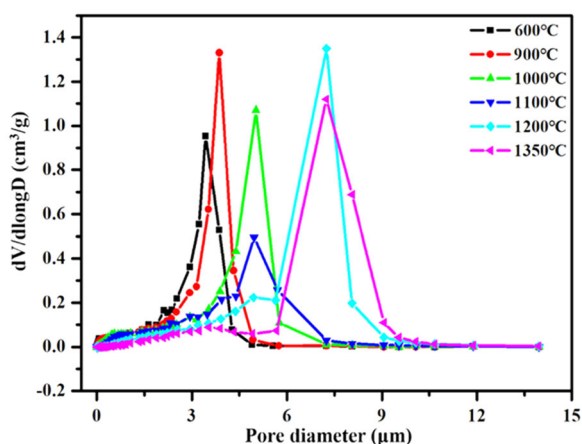
Fig. 5 Pore diameter distribution curves of PCMM at various heat-treatment temperatures. 600 °C (black), 900 °C (red), 1000 °C (green), 1100 °C (blue), 1200 °C (cyan), 1350 °C (magenta).

Table 2. Pore parameter of PCMM at various heat-treatment temperatures.

Sample/pore parameter	Total pore area (m²/g)	Total pore volume (cm³/g)	Porosity (%)	Density (g/mL)
600 °C	1.443	0.218	46.83%	4.050
900 °C	1.915	0.235	48.61%	4.030
1000 °C	0.740	0.214	44.42%	3.738
1100 °C	0.453	0.168	35.12%	3.221
1200 °C	0.187	0.171	37.51%	3.511
1350 °C	0.072	0.164	39.24%	3.948

phases[18,22]. Upon further increasing the heat-treatment temperature from 900 to 1200 °C, ZrO_2 began to react with Ti_3Al and TiAl, creating spherical TiO, Ti_2O_3, TiO_2, Al_2O_3, NbO_2, Nb_2O_5, Zr, ZrO, and ZrO_2. The occurrence of further phase transformation could result in further increase of average pore diameter from 3.95 μm to 7.24 μm. The skeletal structure was further homogenized with concurring dimensional shrinkages to form a hierarchical micro/nano-dual-scaled porous structure at 1350 °C with a final average pore diameter of 7.25 μm. In addition, detailed pore parameters of the PCMM with the addition of 4 wt.% ZrO_2 are given in Table 2.

Fig. 6 provides typical FESEM images of Ti-48Al-6Nb porous alloy and PCMM with 4 wt.% Nano-ZrO_2 addition. As shown in Fig. 6a and b, the Ti-48Al-6Nb porous alloy mainly exhibits irregular spherical interconnected particles and the formation of a microporous skeleton. Unlike the Ti-48Al-6Nb porous alloy, however, smaller pores were observed in the PCMM (with 4 wt.% Nano-ZrO_2 addition), forming nano-sized pores on the inner cell walls of the Ti-48Al-6Nb microporous skeleton (Fig. 6c, d). It is of interest to note that the hierarchical micro/nano-dual-scaled pore structure of porous ceramics was reported to be beneficial to the capturing of high-temperature PM[37–40] because of the effectively increased contact area between PM and porous structures. However, the reported hierarchical micro/nano-dual-scaled porous structures were fabricated by combining chemical grafting of pore-forming agents and polyurethane, which could be easily ablated under high temperature, a potential detriment to practical application[39,40].

High-temperature oxidation and sulfidation performance of composite microfiltration membrane

Given that corrosion and oxidation are key challenges for porous materials application under rigorous conditions, two typical intermetallic porous materials (Ti-48Al and Ti48Al6Nb porous alloys) were also included in our study for comparison with the PCMM. Shown in Fig. 7 are the isothermal oxidation kinetics curves of Ti-48Al, Ti-48Al-6Nb porous alloys and PCMM (with 4 wt.% Nano-ZrO_2 addition) at 900 °C. The obtained mass gain of the Ti-48Al and the Ti-48Al-6Nb porous alloys were 35.024 g/m² and 10.231 g/m², respectively, after 900 °C/100 h isothermal oxidation treatment, whereas the PCMM might characterize a relatively more sluggish high-temperature oxidation kinetics with a mass gain of only 3.235 g/m². The isothermal oxidation results obtained at 900 °C confirmed the beneficial effect of Nano-ZrO_2 introduction on the practical application potential of TiAl-based porous alloys for gas/solid or liquid/solid separation with a broadened operation window. This could be the result of a large amount of various ceramic foams and the higher porosity, which leads to a lower thermal conductivity based on Effective Medium Theory, consistent with the previous work by Smith and Mohanta[41,42].

The pore structure stability, i.e., oxidation/sulfidation resistivity of the PCMM was studied at 900 °C and compared with the Ti-48Al and the Ti-48Al-6Nb porous alloys, the most popular intermetallic porous materials for high-temperature applications[43,44]. Fig. 8 shows that the open pores of Ti-48Al and Ti-48Al-6Nb porous alloys are completely blocked by oxidation/sulfidation products within a 100 h and a 10 h test, respectively, possibly attributable to the large-sized TiO_2 grains formed on the entire surfaces of the Ti-48Al and Ti-48Al-6Nb porous alloy (Fig. 8a and c), consistent with our previous work[45,46]. The PCMM, however, maintained the structural integrity with no obvious pore size variation under the same testing condition (Fig. 8e), possibly attributable to the favorable presence of Al_2O_3, TiO, Ti_2O_3, TiO_2, NbO_2, Nb_2O_5, Zr, ZrO, ZrO_2 particles that hinders the mutual diffusion of oxygen and titanium during high-temperature oxidation. This finding is consistent with the energy dispersion spectrometry (EDS) composition of surface scans of Ti-48Al, Ti-48Al-6Nb porous alloys, and PCMM results shown in Table 3.

The high-temperature sulfidation behavior of the Ti-48Al, Ti-48Al-6Nb porous alloys, and PCMM with the addition of 4 wt.% Nano-ZrO_2 were also investigated with the corresponding results shown in Fig. 8b, d, f. Fig. 8b shows that the Ti-48Al porous alloy was severely corroded with all the pores covered by the small-sized TiO_2 grains after undertaking a 10 h isothermal sulfidation at 900 °C. As for the Ti-48Al-6Nb porous alloy, the multiple corroded areas are detectable with some pores also blocked by the formation of the TiO_2 and Al_2O_3 mixture, though predominantly of TiO_2 (Fig. 8d). With respect to the PCMM, however, most of the pores are retained even though corrosion still appears to have occurred (Fig. 8f). Furthermore, surface composition of samples subjected to sulfidation are analyzed by EDS with the corresponding results listed in Table 4, showing the presence of only Ti and O. For the Ti-48Al-6Nb porous alloy, however, Al and Nb were also identifiable. As for the PCMM, the amount of Al has significantly increased possibly due to its high sulfidation resistance.

Filtration performance of PCMM

Ti-48Al-6Nb porous alloy and PCMM with the addition of 4 wt.% Nano-ZrO_2 were tested (750 °C, 4000 Pa), with the results shown in Fig. 9a. The removal efficiency was calculated using Eq. (1):

$$\eta = 1 - \xi1/\xi2 \times 100\% \qquad (1)$$

where $\xi1$ and $\xi2$ represent the concentrations of incense PM in the downstream and upstream of the filter, respectively. During the experiment, the PM-containing air flows at a constant velocity of 2 L/min through the samples with an effective area of ~1256 mm² (sample specifications: $\Phi40 \times 2.4$ mm), as shown in
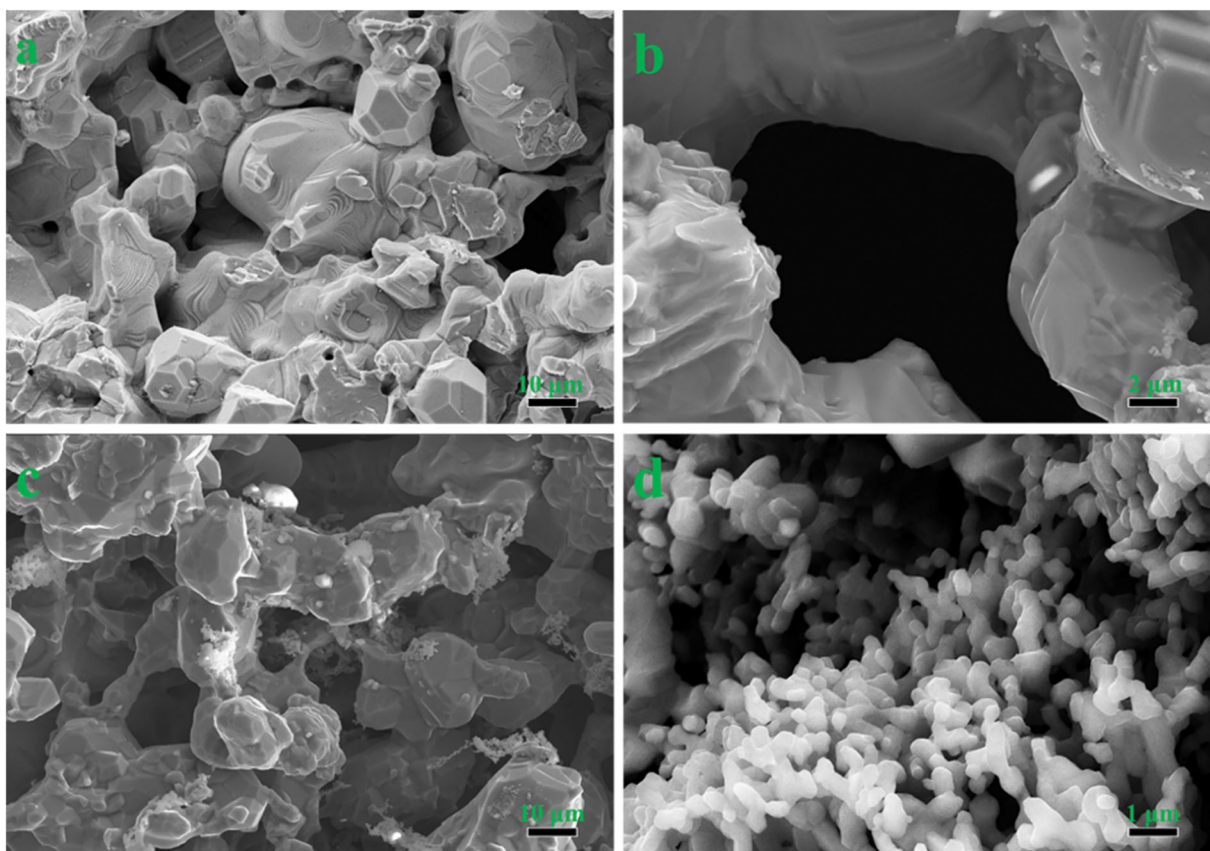
Fig. 6 FESEM image of porous sample. Ti-48Al-6Nb porous alloy: **a** surface; **b** cross-sectional; PCMM: **c** surface; **d** cross-sectional.
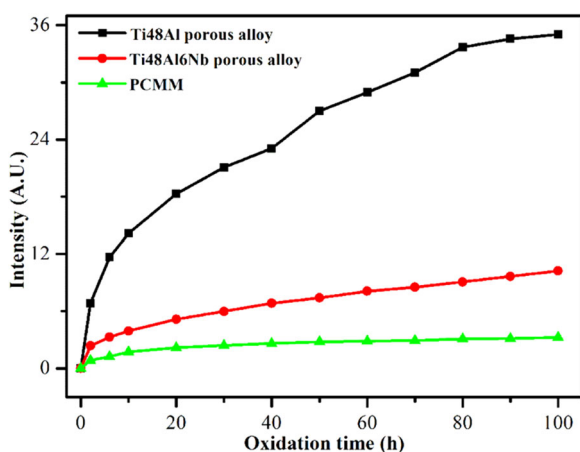

Fig. 7 Mass gain of porous sample at 900°C. Ti-48Al porous alloy (black), Ti-48Al-6Nb porous alloy (red), and PCMM with 4 wt.% Nano-ZrO_2 addition (green).

Fig. 9b and c. The PM concentration after filtration using Ti-48Al-6Nb porous alloy or PCMM filtration is much lower than the concentration before filtration in both cases (Fig. 9d). For PM with sizes >2.5 μm, the removal efficiency does not vary significantly for Ti-48Al-6Nb porous alloy or PCMM, although the separation efficiencies can be enhanced to 99.58% and 99.98% from 97.38% and 97.89% for $PM_{2.5-5}$ and PM_{5-10}, respectively. However, for PM with sizes <2.5 μm, the removal efficiency of PCMM is found to be greatly increased to 99.23%, 98.51%, 91.36% and 79.66% from 85.03%, 43.54%, 23.63% and

5.13% corresponding to $PM_{1-2.5}$, $PM_{0.5-1}$, $PM_{0.3-0.5}$, $PM_{<0.3}$, respectively, as shown in Fig. 9e.

The high-temperature PM (including $PM_{>2.5 \text{ μm}}$, $PM_{<2.5 \text{ μm}}$) was filtered and compared through Ti-48Al-6Nb porous alloy and PCMM with 4 wt.% Nano-ZrO_2 addition. The test was conducted for 60 min at an airflow rate of 2 L/min, with the results shown in Fig. 10 confirming that both high-temperature $PM_{<2.5 \text{ μm}}$ and $PM_{>2.5 \text{ μm}}$ can be filtered through Ti-48Al-6Nb membrane with a separation efficiency of 33.32% (SD: ± 0.28%) and 97.46% (SD: ± 0.41%), respectively. In contrast, the high-temperature $PM_{<2.5}$ and $PM_{>2.5}$ separation efficiencies can be enhanced to 91.25% (SD: ± 0.21%) and 99.58% (SD: ± 0.22%) when using PCMM. Furthermore, comparison between our PCMM and various porous materials in previous studies[38–40,47,48] shows that our PCMM with a hierarchical micro/nano-dual-scaled pore structural feature exhibits a relatively higher $PM_{>2.5 \text{ μm}}$ removal efficiency at a much higher pressure (refer to Table 5). It is of note that the upper limit of service temperature of the as-prepared PCMM could be much higher than the testing temperature since PCMM could survive a temperature of up to 900 °C. These results indicate that our PCMM with hierarchical micro/nano-dual-scaled porous structure can achieve flow-through filtration with high removal efficiency, showing great commercialization prospects for high-temperature PM filtration.

The PM filter model of as-prepared Ti-48Al-6Nb porous alloy and PCMM are proposed and schematically illustrated in Fig. 11. The capturing of $PM_{2.5}$ by conventional porous materials, is much more challenging because of the ultra-low mass and small particle size of $PM_{2.5}$[49]. Conventional filters characteristic of regular pores could obstruct to the PM-transport, and effectively intercept larger PM. For the as-prepared Ti-48Al-6Nb porous alloy, the minimum filterable particle size is determined by "the size of the pore-throat" in the pore tunnel, and exhibits inferior
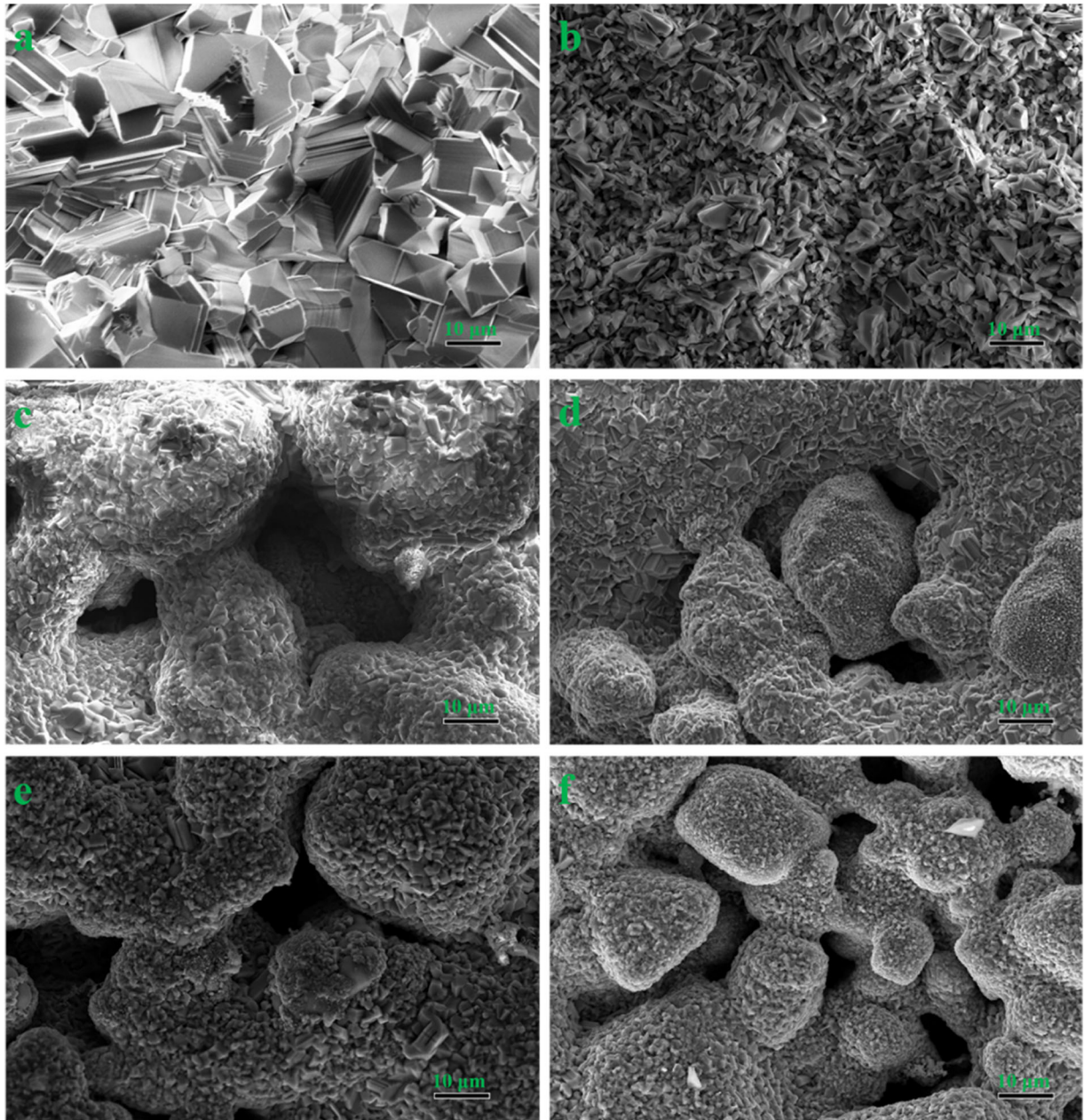
Fig. 8 FESEM images of porous materials treated by isothermal oxidation and isothermal sulfidation. a, b Ti-48Al porous alloy; **c, d** Ti-48Al-6Nb porous alloy; **e, f** PCMM with 4 wt.% Nano-ZrO$_2$.

Table 3. EDS composition analysis of porous sample after isothermal oxidation treatment.

Sample	O	Al	Ti
Ti-48Al porous alloy	68.83	0.18	30.99
Ti-48Al-6Nb porous alloy	59.43	6.88	33.68
PCMM	44.38	21.71	33.91

Table 4. EDS composition analysis of porous sample after isothermal sulfidation treatments.

Sample	O	Al	Ti	Nb
Ti-48Al	66.54	0	33.46	0
Ti-48Al-6Nb	64.79	3.93	31.75	0.53
PCMM	60.50	15.21	23.86	0.43

filtration performance for PM$_{<2.5}$, because PM with a diameter <2.5 μm could easily pass through its large pore-throat without being captured (Fig. 11 a). Compared with the Ti-48Al-6Nb porous alloy, the filtering efficiency of PCMM was greatly improved benefited from the smaller pores fabricated on the inner cell walls through our approach of chemical reaction

between Nano-ZrO$_2$ and Ti$_3$Al/TiAl at 900–1350 °C, effectively forming a hierarchical micro/nano-dual-scaled porous structure (Fig. 11 b). The PCMM with hierarchical micro/nano-dual-scaled porous structure by combining diffusion forming and chemical reaction forming technologies demonstrates potential for
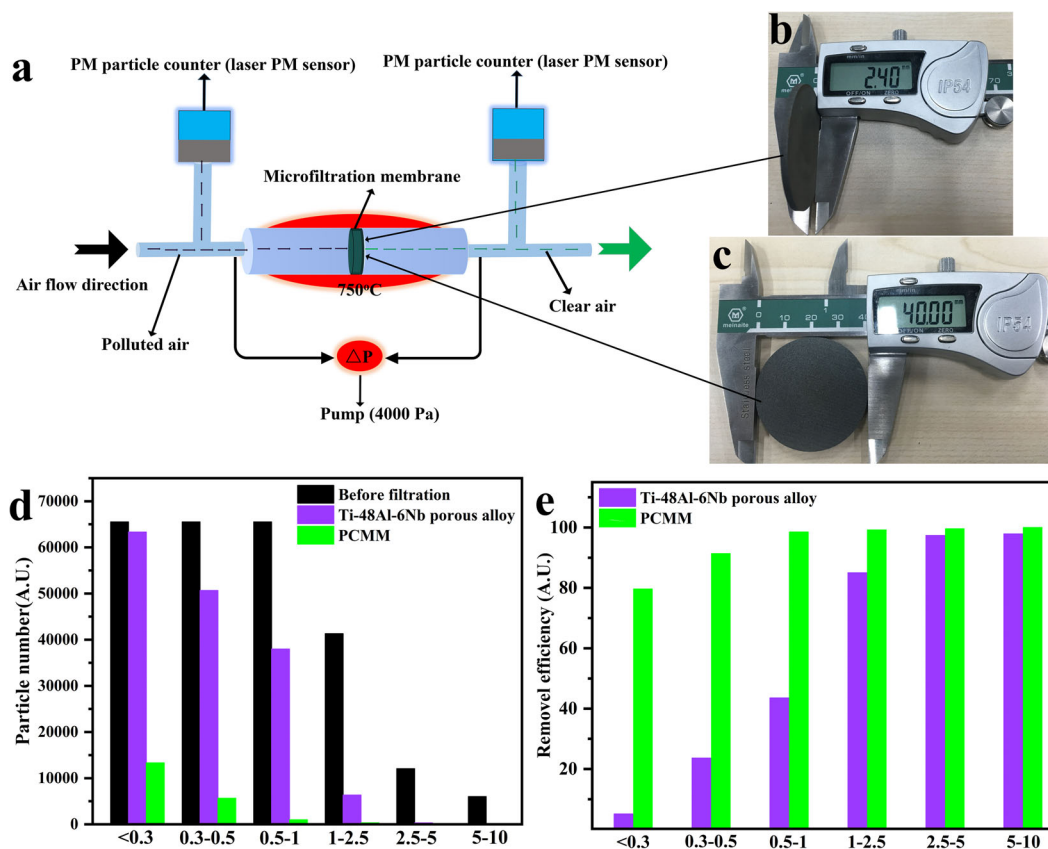
Fig. 9 High-temperature filtration performance test of porous sample. a Schematic of high-temperature PM filtration setup. **b**, **c** The pictures of PCMM sample; **d** PM concentration of dust-laden smoke (original) and after filtration under test condition; **e** removal efficiency.
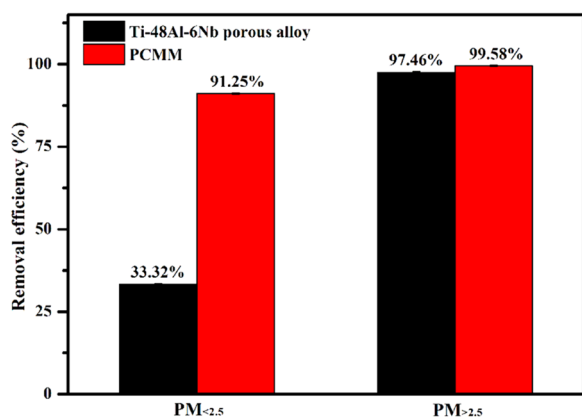
Fig. 10 Removal efficiency of porous sample. Ti-48Al-6Nb porous alloy (black) and PCMM (red) after 60 min filtration test.

applications in environment related fields where highly effective and robust high-temperature filtration is required.

METHODS

Materials

Ti, Al, and Nb powders (99.9%) with an average particle size of <50 μm and ZrO$_2$ nanoparticles (99.9%) with an average particle size of less than 50 nm were used, purchased from Beijing DK nano technology Co., LTD.

Characterization analysis

XRD (Multipurpose X-ray Diffractometer TTR III) and XPS (Thermo Kalpha) were used to analyze the phase formation and crystal structure of Ti-48Al-6Nb

porous alloy and the PCMM. The morphological features of Ti-48Al-6Nb porous alloy and PCMM were investigated using FESEM (ZEISS SUPRA55), whereas the surface composition analysis of the Ti-48Al-6Nb porous alloy and PCMM were performed by applying EDS. The pore parameters of the Ti-48Al-6Nb porous alloy and the PCMM were measured using mercury intrusion porosimetry (MIP, Quantachrome AUTOSCAN-33). The weights of Ti-48Al-6Nb porous alloy and PCMM were measured using a METTLER TOLEDO XSE electronic analytical balance with an accuracy of ±0.01 mg. Laser PM sensor (A4-CG; YEETC Co., Ltd, Beijing, China) was used to measure particle size and number before and after filtration.

Preparation of PCMM

PCMM was prepared using a modified powder metallurgy method as described below. Commercial Ti, Al, and Nb powders (average particle sizes of <50 μm) with the atomic ratio of 46:48:6 were mixed with 0.5–8 wt.% Nano-ZrO$_2$ (average particle sizes of <50 nm) by ball milling at 130 rpm in a ball crusher for 10 h (ball-to-powder weight ratio of 5:1), then pressed into green pellets with a diameter of 20 mm under the pressure of 200 MPa. Subsequently, a four-step heat-treatment under vacuum was carried out to fabricate PCMM (120 °C/1 h, 600 °C/3 h, 900 °C/3 h, 1350 °C/3 h). The Ti-48Al and Ti-48Al-6Nb porous alloys obtained from the same processing procedures without any addition of Nano-ZrO$_2$ was also prepared for comparison.

Isothermal oxidation and isothermal sulfidation tests

Isothermal oxidation tests were conducted in a quartz tube furnace. The isothermal oxidation behaviors of the Ti-48Al, Ti-48Al-6Nb porous alloys and PCMM (with 4 wt.% Nano-ZrO$_2$ addition) were observed at 900 °C for 100 h. All the samples were tested at 900 °C for high-temperature oxidation, removed from the furnace at various oxidation intervals (2, 5, 10, 20, 30, 40, 50, 60, 70, 80, 90, and 100 h), cooled in air for 1 h for weighing, and then, where applicable, placed back into the furnace for continued oxidation until 100 h. The isothermal sulfidation behavior of Ti-48Al porous alloy, Ti-48Al-6Nb porous alloy, and PCMM were observed at

Table 5. Comparison of $PM_{>2.5\,\mu m}$ removal performance of PCMM with reported results.

Sample name	Airflow ratio (L/min)	Removal efficiency (%)	Pressure drop (Pa)	Test temperature (°C)	References
Polyimide-nanofiber		95.5	80	370	38
Alumina foams	8	94.2	50	750	39
SiC ceramic foam	14	60	600	750	40
PP/MgSt melt blown					
Nonwoven	85	99.2	92	200	47
PEO/POHABA fiber membrane	45	99.2		25	48
PCMM	2	99.58	4000	750	This work
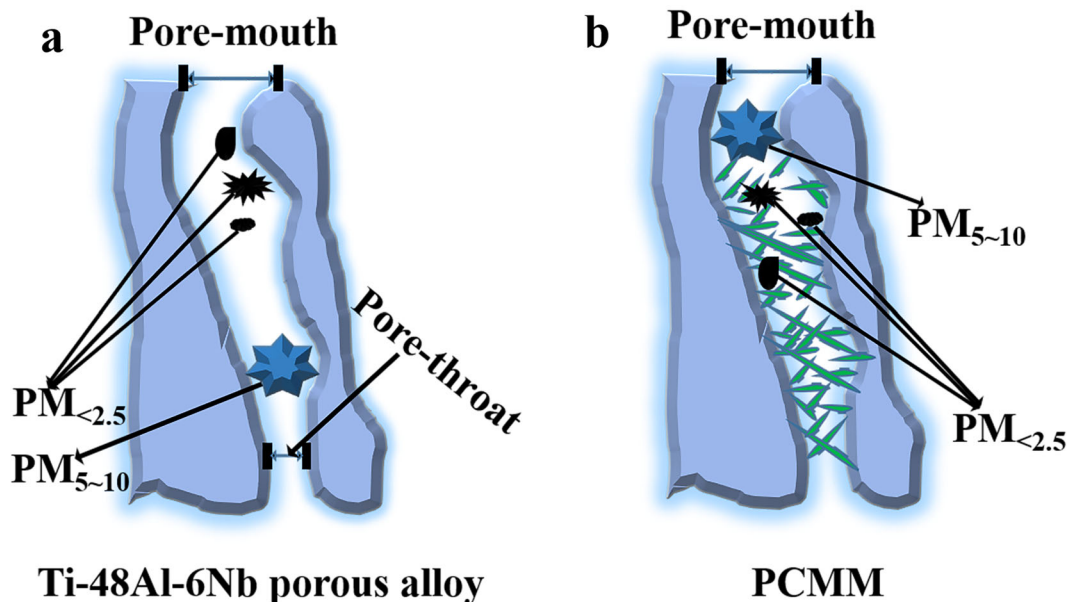
Fig. 11 Schematic illustration of PM removal mechanism for as-prepared porous sample. a Ti-48Al-6Nb porous alloy; **b** PCMM.

900 °C for 10 h. All the samples were tested at 900 °C for high-temperature sulfidation with continuous ventilation of SO_2 gas of 99% in purity, removed from the furnace with a total sulfidation duration of 10 h, cooled in air for 2 h before further characterizations, and the residual SO_2 gas was removed using saturated sodium hydroxide aqueous solution.

High-temperature filtration performance tests. An in-house air filtration apparatus was applied to evaluate the filtration performances. The PM in the current experiment was generated by burning incense[50], whereas the size and concentration of PM before and after filtration were measured by two laser PM sensors. During the experiment, the PM-containing air flows at a 2 L/min constant velocity through the samples with an effective area of about 1256 mm^2 (sample specifications: Φ40 × 2.4 mm). Nine samples divided into three groups from each Ti-48Al-6Nb porous alloy and PCMM with 4 wt.% Nano-ZrO_2 addition were tested to ensure filtration measurement accuracy.

DATA AVAILABILITY
The authors declare that the data supporting the findings of this study are available within the paper.

REFERENCES
1. Nel, A. Air pollution-related illness: effects of particles. *Science* **308**, 804 (2005).
2. Fang, D. L. et al. Clean air for some: unintended spillover effects of regional air pollution policies. *Sci. Adv.* **5**, eaav4707 (2019).
3. Schmale, J., Shindell, D., Schneidemesser, E. V., Chabay, I. & Lawrence, M. Air pollution: clean up our skies. *Nature* **515**, 335 (2014).
4. Squires, A. M. Clean fuels from coal gasification. *Science* **184**, 340 (1974).
5. Liu, C. et al. Transparent air filter for high-efficiency PM2.5 capture. *Nat. Commun.* **6**, 6205 (2015).
6. Lee, J., Theis, J. R. & Kyriakidou, E. A. Vehicle emissions trapping materials: successes, challenges, and the path forward. *Appl Catal. B-Environ.* **243**, 397 (2019).
7. Pope, C. A. & Dockery, D. W. Health effects of fine particulate air pollution: lines that connect. *J. Air Waste Manag. Assoc.* **56**, 709 (2006).
8. Anenberg, S. C., Horowitz, L. W., Tong, D. Q. & West, J. J. An estimate of the global burden of anthropogenic ozone and fine particulate matter on premature human mortality using atmospheric modeling. *Environ. Health Perspect.* **118**, 1189 (2010).
9. Brook, R. D. et al. Particulate matter air pollution and cardiovascular disease an update to the scientific statement from the american heart association. *Circulation* **121**, 2331 (2010).
10. Wu, W. et al. Association of cardiopulmonary health effects with source-appointed ambient fine particulate in Beijing, China: a combined analysis from the Healthy Volunteer Natural Relocation (HVNR) study. *Environ. Sci. Technol.* **48**, 3438 (2014).
11. Betha, R., Behera, S. N. & Balasubramanian, R. 2013 southeast asian smoke haze: fractionation of particulate-bound elements and associated health risk. *Environ. Sci. Technol.* **48**, 4327 (2014).
12. Banhart, J. Manufacture, characterisation and application of cellular metals and metal foams. *Prog. Mater. Sci.* **46**, 559 (2001).
13. Luo, X. L. et al. Two functional porous metal-organic frameworks constructed from expanded tetracarboxylates for gas adsorption and organosulfurs removal. *Cryst. Growth Des.* **16**, 7301 (2016).
14. Kitaoka, S., Matsushima, Y., Chen, C. & Awaji, H. Thermal cyclic fatigue behavior of porous ceramics for gas cleaning. *J. Am. Ceram. Soc.* **87**, 906 (2004).
15. Voigt, C. et al. Reticulated porous foam ceramics with different surface chemistries. *J. Am. Ceram. Soc.* **97**, 2046 (2014).

16. Liu, J. J., Li, Y. B., Li, Y. W., Sang, S. B. & Li, S. J. Effects of pore structure on thermal conductivity and strength of alumina porous ceramics using carbon black as pore-forming agent. *Ceram. Int.* **42**, 8221 (2016).

17. Zhang, G. H. et al. High-performance particulate matter including nanoscale particle removal by a self-powered air filter. *Nat. Commun.* **11**, 2020 (1653).

18. He, Y. H. et al. Fabrication of Ti-Al micro/nanometer-sized porous alloys through the Kirkendall effect. *Adv. Mater.* **19**, 2102 (2007).

19. Chen, G. et al. Polysynthetic twinned TiAl single crystals for high-temperature applications. *Nat. Mater.* **15**, 876 (2016).

20. Yao, J. Q., He, Y. D., Wang, D. R. & Lin, J. P. High-temperature oxidation resistance of (Al$_2$O$_3$-Y$_2$O$_3$)/(Y$_2$O$_3$-stabilized ZrO$_2$) laminated coating on 8Nb-TiAl alloy prepared by a novel spray pyrolysis. *Corros. Sci.* **80**, 19 (2014).

21. Rackel, M. W. et al. Orthorhombic phase formation in a Nb-rich γ-TiAl based alloy- An in situ synchrotron radiation investigation. *Acta Mater.* **121**, 343 (2016).

22. Wang, F., Liang, Y. F., Shang, S. L., Liu, Z. K. & Lin, J. P. Phase transformation in Ti-48Al-6Nb porous alloys and its influence on pore properties. *Mater. Des.* **83**, 508 (2015).

23. Zhang, D. Q., Wu, J. Y., Li, B. & Fan, Y. Q. Preparation of ceramic membranes on porous Ti-Al alloy supports by an in-situ oxidation method. *J. Membr. Sci.* **476**, 554 (2014).

24. Yang, F. et al. Pore structure and gas permeability of high Nb-containing TiAl porous alloys by elemental powder metallurgy for microfiltration application. *Intermetallics* **33**, 2 (2013).

25. Jiao, X. Y., Feng, P. Z., Wang, J. Z., Ren, X. R. & Akhtar, F. Exothermic behavior and thermodynamic analysis for the formation of porous TiAl$_3$ intermetallics sintering with different heating rates. *J. Alloy. Compd.* **811**, 152056 (2019).

26. Jiang, Y., He, Y. H. & Liu, C. T. Review of porous intermetallic compounds by reactive synthesis of elemental powders. *Intermetallics* **93**, 217 (2018).

27. Guinée, J. B., Heijungs, R., Vijver, M. G. & Peijnenburg, W. J. G. M. Setting the stage for debating the roles of risk assessment and life-cycle assessment of engineered nanomaterials. *Nat. Nanotechnol.* **12**, 727 (2017).

28. Cheng, S. W. et al. Big effect of small nanoparticles: a shift in paradigm for polymer nanocomposites. *Acs Nano* **11**, 752 (2017).

29. Deloid, G. M., Cohen, J. M., Pyrgiotakis, G. & Demokritou, P. Preparation, characterization, and in vitro dosimetry of dispersed, engineered nanomaterials. *Nat. Protoc.* **12**, 355 (2017).

30. Yao, J. Q. et al. Thermal barrier coating bonded by (Al$_2$O$_3$-Y$_2$O$_3$)/(Y$_2$O$_3$-stabilized ZrO$_2$) laminated composite coating prepared by two-step cyclic spray pyrolysis. *Corros. Sci.* **80**, 37 (2014).

31. Jiang, P. et al. Thermal-cycle dependent residual stress within the crack-susceptible zone in thermal barrier coating system. *J. Am. Ceram. Soc.* **101**, 4256 (2018).

32. Biesinger, M. C., Lau, L. W. M., Gerson, A. R. & Smart, R. S. C. Resolving surface chemical states in XPS analysis of first row transition metals, oxides and hydroxides: Sc, Ti, V, Cu and Zn. *Appl. Surf. Sci.* **257**, 887 (2010).

33. Auciello, O. et al. Hybrid titanium-aluminum oxide layer as alternative high-k gate dielectric for the next generation of complementary metal-oxide-semiconductor devices. *Appl. Phys. Lett.* **86**, 1 (2005).

34. Yamamoto, T., Nanbu, F., Tanaka, T. & Kawai, J. Quantitative chemical state analysis of supported vanadium oxide catalysts by high resolution vanadium Kα spectroscopy. *Anal. Chem.* **83**, 1681 (2011).

35. Zhou, P. et al. Effect of concurrent joule heat and charge trapping on RESET for NbAlO fabricated by atomic layer deposition. *Nanoscale Res. Lett.* **8**, 91 (2013).

36. Reddy, B. M. et al. Characterization of V$_2$O$_5$/TiO$_2$-ZrO$_2$ catalysts by XPS and other techniques. *J. Phys. Chem. B* **102**, 10176 (1998).

37. Han, L. et al. Foam-gelcasting preparation, microstructure and thermal insulation performance of porous diatomite ceramics with hierarchical pore structures. *J. Eur. Ceram. Soc.* **37**, 2717 (2017).

38. Zhang, R. F. et al. Nanofiber air filters with high-temperature stability for efficient PM$_{2.5}$ removal from the pollution sources. *Nano Lett.* **16**, 3642 (2016).

39. Liu, J. J. et al. Novel design of alumina foams with three-dimensional reticular architecture for effective high-temperature particulate matter capture. *J. Am. Ceram. Soc.* 1 (2019).

40. Meloni, E., Caldera, M., Palma, V., Pignatelli, V. & Gerardi, V. Soot abatement from biomass boilers by means of open-cell foams filters. *Renew. Energy* **131**, 745 (2019).

41. Smith, D. S. et al. Thermal resistance of grain boundaries in alumina ceramics and refractories. *J. Am. Ceram. Soc.* **86**, 105 (2003).

42. Mohanta, K., Kumar, A., Parkash, O. & Kumar, D. Low cost porous alumina with tailored microstructure and thermal conductivity prepared using rice husk and sucrose. *J. Am. Ceram. Soc.* **97**, 1708 (2014).

43. Yoshihara, M. & Kim, Y.-W. Oxidation behavior of gamma alloys designed for high temperature applications. *Intermetallics* **13**, 952 (2005).

44. Kim, D. et al. Oxidation behaviour of gamma titanium aluminides with or without protective coatings. *Int. Mater. Rev.* **59**, 297 (2014).

45. Zhao, L. L. et al. Influence of Y addition on the long time oxidation behaviors of high Nb containing TiAl alloys at 900 ℃. *Intermetallics* **18**, 1586 (2010).

46. Gui, W. Y. et al. High Nb-TiAl-based porous composite with hierarchical micro-pore structure for high temperature applications. *J. Alloy. Compd.* **744**, 263 (2018).

47. Zhang, H., Liu, J., Zhang, X., Huang, C. & Jin, X. Design of electret polypropylene melt blown air filtration material containing nucleating agent for effective PM$_{2.5}$ capture. *RSC Adv.* **8**, 7932 (2018).

48. Su, Y. C. et al. Necklace-like fiber composite membrane for high-efficiency particulate matter capture. *Appl. Surf. Sci.* **425**, 220 (2017).

49. Lalagiri, M. et al. Filtration efficiency of submicrometer filters. *Ind. Eng. Chem. Res.* **52**, 16513 (2013).

50. Zuo, F. L. et al. Free-standing polyurethane nanofiber/nets air filters for effective PM capture. *Small* **13**, 1702139 (2017).

ACKNOWLEDGEMENTS

AUTHOR CONTRIBUTIONS

The idea was proposed by Wanyuan Gui and Junpin Lin. The experiments were carried out by Wanyuan Gui and Yuhai Qu. The experimental results were analyzed and interpreted by Wanyuan Gui, Yongfeng Liang, Yanli Wang, Hui Zhang, and Junpin Lin. Wanyuan Gui and Junpin Lin wrote the main manuscript. XPS analysis was suggested by Benli Luan, and the manuscript was reviewed by Junpin Lin and Benli Luan.

COMPETING INTERESTS

The authors declare no competing interests.

ADDITIONAL INFORMATION

Correspondence and requests for materials should be addressed to B.L. or J.L.

Reprints and permission information is available at http://www.nature.com/reprints

Publisher's note Springer Nature remains neutral with regard to jurisdictional claims in published maps and institutional affiliations.